Spectroscopic imaging with volume selection by unpaired adiabatic π pulses: Theory and application

Julien Valette *, Jang-Yeon Park, Olli Gröhn, Kāmil Uǧurbil,
Michael Garwood, Pierre-Gilles Henry

Center for Magnetic Resonance Research, Department of Radiology, University of Minnesota, 2021 Sixth Street SE, Minneapolis, MN 55455, USA

Abstract

In NMR spectroscopy, volume selection can be advantageously achieved using adiabatic π pulses, which enable high bandwidth and B_1 insensitivity. In order to avoid the generation of non-linear phase profiles and the subsequent signal loss caused by incoherent averaging, adiabatic π pulses are usually used in pairs for volume selection in each spatial dimension. Alternatively, when performing spectroscopic imaging (SI), a high enough spatial resolution results in negligible phase dispersion within each pixel. This allows using only one pulse per selected spatial dimension, resulting in a reduced echo-time and reduced power deposition. In this work, the feasibility of such an approach is explored theoretically and numerically, allowing the derivation of explicit conditions to obtain SI images without artifact. Adequate spatial and spectral post-processing procedures are described to compensate for the effect of non-linear phase profiles. These developments are applied to SI in the rat brain at 9.4 T, using a new adiabatic sequence named Pseudo-LASER.
Published by Elsevier Inc.

Keywords: Spectroscopic imaging; Adiabatic pulse; Non-linear phase; Spatial response function; Reconstruction

1. Introduction

Spectroscopic imaging (SI) [1] of the brain combined with volume selection allows minimization of spectral contamination by lipid signal from the scalp, which overlap with metabolite resonances. Compared to conventional volume selection using, for example, STEAM or PRESS [2,3], prelocalization can be advantageously achieved using adiabatic pulses, leading to excellent insensitivity to B_1 inhomogeneity and to reduced chemical shift displacement error due to the high achievable bandwidth of adiabatic pulses [4].

An example of fully adiabatic localization sequence is the LASER sequence [4], which can be used for SI prelocalization [5,6]. In this sequence, after a non-selective excitation using an adiabatic half-passage (AHP) pulse

(π/2 rotation), volume selection along the three spatial dimensions is achieved by three pairs of adiabatic full-passage (AFP) pulses (π rotation) in conjunction with B_0 gradients. The necessity to use a pair of AFP pulses in each dimension arises from the fact that the π rotation induced by a single AFP pulse generates a non-linear phase in the direction orthogonal to the selected slab, which results in net signal loss due to incoherent averaging of the magnetization. The non-linear phase is refocused by another identical AFP pulse with B_0 gradient in the same direction [7,8], hence restoring full signal coherence, but at the expense of an increased echo-time (TE) and increased power deposition.

However, when imaging a volume of interest (VOI) prelocalized by unpaired adiabatic pulses, non-linear phase dispersion results in negligible signal loss provided intra-pixel phase variation is small enough, as it is usually the case in MRI [9–12]. In addition to the shorter TE and the lower power deposition associated to a single adiabatic pulse, the fact that magnetization is never in phase even at

---

* Corresponding author. Fax: +1 612 626 2004.
  E-mail address: julien@cmrr.umn.edu (J. Valette).

the center of the *k*-space may result in a higher signal-to-noise ratio (SNR) due to a more efficient use of the analog-to-digital converter, as pointed out in the general case of phase scrambling [13,14].

In the context of SI, VOI selection by unpaired adiabatic pulses was first described in the work of Gröhn and Garwood in the cat brain [15], followed by Sacolick et al. in the human brain [16]. In both cases, *in vivo* 2D-SI experiments were performed using an octagonal localization scheme: four slabs were successively selected in partially overlapping orientations (0°, 45°, 90° and 135°) by single AFP pulses, resulting in partial refocusing. One advantage of such a localization scheme is the more flexible VOI shape compared to a rectangular shape, without requiring more pulses (i.e. four AFP pulses for 2D volume selection). Another advantage is that the partial phase refocusing throughout the VOI yields data that are very similar to regular, in-phase data, so that standard reconstruction may be efficient. However, the method neither allows a net TE and power reduction, nor a potentially beneficial phase scrambling.

In this context, the aim of the present work is to explore the feasibility of SI using only one AFP pulse for VOI selection in each phase-encoded direction. Theoretical considerations are developed about the properties associated to a non-linear phase profile, the conditions to obtain a correct image are pointed out, and adequate spatial and spectral post-processing is presented. These developments are then evaluated by numerical simulation. Finally, a new adiabatic sequence allowing selection with unpaired AFP pulses along two orthogonal dimensions, named Pseudo-LASER, is used for 2D-SI in the rat brain at 9.4 T.

2. Theory

The usual notation $k = \gamma \int G(t)\,dt$ is used, with k in radian per length unit. Only one spatial dimension is considered in the following, but all results can be extended to 2D or 3D. Let us assume a spin distribution with density $\rho(x,\delta)$, and let $\Phi(x,\delta)$ be the phase distribution induced by the pulse, where x is the position and δ the chemical shift. The effect of chemical shift will be generally neglected when considering Φ, given the usual high bandwidth of adiabatic pulses compared to the δ range. In consequence the dependence of $\rho(x,\delta)$ on δ will also be omitted for clarity. The resulting complex function to be imaged is therefore $\rho(x)\exp(i\Phi(x))$, which can ideally be retrieved by inverse Fourier transform of the Fourier components as measured by the phase-encoding scheme. However, the fact that the distribution has a spatially varying phase induces some special properties in the practical context of sparse *k*-space sampling.

2.1. Spatial response function

The localization accuracy is fully characterized by the spatial response function (SRF), which is defined as the contribution of any position x to the signal of the pth pixel (centered around x_p). Strictly speaking, the SRF only depends on the *k*-space sampling scheme. However, since the non-linear phase induced by unpaired AFP pulses is intrinsically associated to the prelocalization, it might as well be incorporated into the SRF description, yielding a generalized SRF describing completely the spatial origin of the signal for the whole localization process (volume selection + SI encoding). The generalized SRF for pixel p (denoted $SRF(x,x_p)$) is obtained by multiplying the nominal SRF (SRF^0) by the non-linear phase distribution:

$$SRF(x,x_p) = e^{i\Phi(x)}SRF^0(x,x_p) \tag{1}$$

The (generalized) SRF for a uniform sampling with $N = 16$ phase encodings is displayed on Fig. 1 for $\Phi(x) = 0$ and for a quadratic phase $\Phi(x) = 32\pi \times (x/FOV)^2$, where x varies between $-FOV/2$ and $FOV/2$ (*FOV*: field of view). For a pixel at the center of the FOV (Fig. 1a), the shape of the main lobe remains unaltered by the non-linear phase, implying that the intra-pixel signal is preserved. In contrast for a pixel near the edge of the FOV (Fig. 1b), signal dephasing results in a narrower lobe and consequently in signal loss. Regarding signal originating from outside the nominal pixel (i.e. from the secondary lobes), an interesting phenomenon appears when the SRF is modulated by $\Phi(x)$: in some regions, the SRF remains positive (or negative) over relatively large regions, so that the signal from these regions adds coherently,
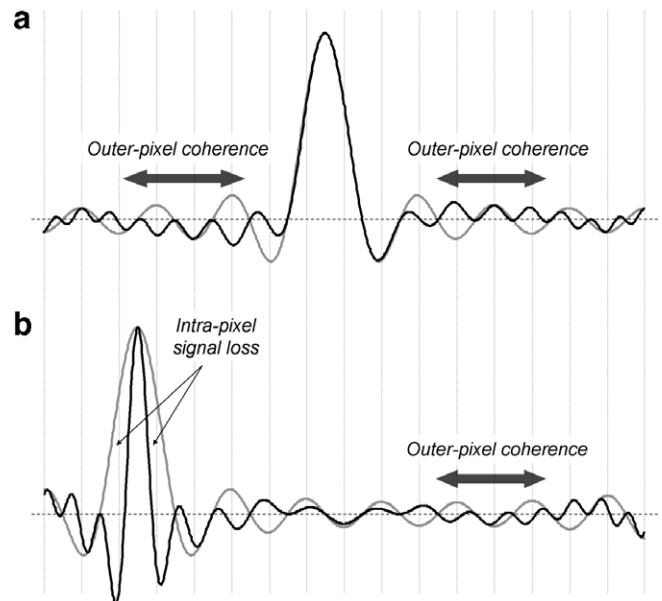

Fig. 1. Spatial response function (SRF) for an uniform *k*-space sampling with $N = 16$ phase encodings, multiplied by a zero phase (gray curve) and a centered quadratic phase $\Phi(x) = 32\pi \times (x/FOV)^2$ (black curve). (a) SRF for the 8th pixel. (b) SRF for the 3rd pixel. While the area under the black curve is preserved in (a), the decrease of the area under the black curve in (b) corresponds to dramatic signal loss. Large outer-pixel coherence regions (where the SRF does not integrate to zero) appear for the black curve in both (a) and (b), at similar positions. Only the real part of the SRF is displayed.

potentially resulting in increased truncation artifacts or contamination. This phenomenon will be referred to as "outer-pixel coherence". The conditions to minimize intra-pixel signal loss and outer-pixel coherence will now be discussed.

2.2. Intra-pixel signal loss

The phase dispersion within each pixel has to be small enough to minimize signal loss [15,16]. In order to estimate this loss, let us model the SRF by a typical cosine-like shape. Developing $\Phi(x)$ to the first order, the signal within the nominal pth pixel (i.e. within the nominal full width at half maximum FWHM) is:

$$|S(x_p)| = \int_{x=-FWHM/2}^{FWHM/2} \cos\left(\frac{2\pi}{3}\frac{x}{FWHM}\right) \times \exp\left(i\frac{\partial\Phi}{\partial x}(x_p)\cdot x\right)dx \tag{2}$$

Here the factor $2\pi/3$ allows the modulus of the SRF to be 0.5 when $x = \pm FWHM/2$. Integration of Eq. (2), and normalization by the case $\partial\Phi/\partial x = 0$, yields the following signal loss within the nominal pixel:

$$\left|\frac{S}{S_0}(x_p)\right| = \frac{\pi}{3\sqrt{3}}\text{sinc}\left(\varphi_p + \frac{\pi}{3}\right) + \frac{\pi}{3\sqrt{3}}\text{sinc}\left(\varphi_p - \frac{\pi}{3}\right) \tag{3}$$

In the equation above we introduced $\varphi_p = (\partial\Phi/\partial x)(x_p) \times FWHM/2$, which is a characteristic phase for the pth pixel, depending both on the phase distribution induced by the pulse and on the k-space sampling *via* the nominal FWHM. Signal loss as a function of φ_p (Eq. (3)) is plotted on Fig. 2. In the following we will consider the 5% signal loss around $\varphi_p = 0.6$ radian as the maximal acceptable loss for SI data, which usually suffer from low SNR (for 2D selection, this results in a $\sim$10% signal loss). Given the definition of φ_p, the condition to obtain an image with negligible signal loss is therefore, with Φ in radian:

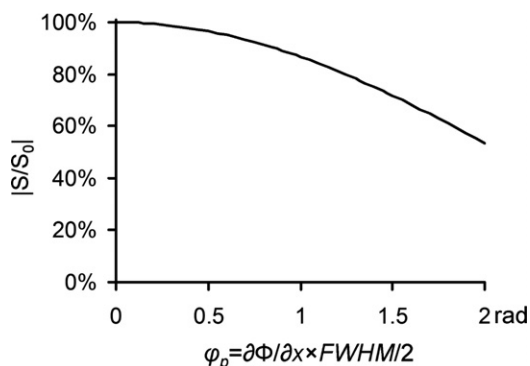$$\left|\frac{\partial\Phi}{\partial x}\right|FWHM \leqslant 1.2 \text{ rad} \tag{4}$$

Fig. 2. Intra-pixel signal loss, as a function of the characteristic phase of the pth pixel $\phi_p = (\partial\Phi/\partial x)(x_p) \times FWHM/2$.

For a uniform k-space weighting (sampled between $-k_{max}$ and k_{max}), the FWHM is $\sim$1.2$\times$ the FOV divided by the number of encoding steps N, or equivalently $1.2\pi/k_{max}$. In this context Eq. (4) yields the following two equivalent conditions:

$$N \geqslant FOV\left|\frac{\partial\Phi}{\partial x}\right| \tag{5}$$

$$\left|\frac{\partial\Phi}{\partial x}\right| \leqslant 0.3k_{max} \tag{6}$$

In Eq. (6), the term $\partial\Phi/\partial x$ appears as an intrinsic spatial frequency at a given position, which has to be smaller than 30% of the maximal sampled spatial frequency. Let us denote this condition C_N. This is a general condition which should be valid whatever the kind of pulse or rotation involved. It is shown in Appendix A that, for a π rotation induced by a hyperbolic secant (HS1) pulse [17,18], for 90% of the selected slab (i.e. excluding the edges), C_N reduces to (with the usual value $\beta = 5.3$ for the HS1 cutoff factor, THK being the thickness of the slab selected by the pulse, and R being the product of the bandwidth BW in Hz by the pulse duration T_p in s):

$$N \geqslant 1.75R\frac{FOV}{THK} \tag{7}$$

Note that Park et al. found that N greater than $R \times FOV/THK$ was enough to yield good images when the HS1 pulse was used for excitation [12]. The fact that this is about twice as low as the minimal N required by the Eq. (7) results from the fact that the non-linear phase induced by a $\pi/2$ rotation is twice as low as the phase induced by a π rotation. Interestingly, in the case of a CHIRP pulse [19], C_N can be shown to be:

$$N \geqslant 8.5R\frac{FOV}{THK} \tag{8}$$

Hence, for a given R, the CHIRP appears to require a much higher number of phase encodings for C_N to be fulfilled. We did not perform the calculation for HSn pulses, however we expect that the minimal number of phase encodings for HSn lies between the values obtained for HS1 and CHIRP pulses and increases with n, since HSn pulses are intermediates between these two kinds of pulse [20].

2.3. Outer-pixel coherence

While intra-pixel signal loss in itself does not modify the localization accuracy, outer-pixel coherence may result in poor localization by signal mixing, which is critical in SI given the small intensity of metabolite signal compared to possible contamination signal (non-suppressed water, lipids...).

The SRF of pixel p for a uniform sampling with zero-phase is $SRF^0(x, x_p) = 1/N \times \sin(\pi N(x - x_p)/FOV)/\sin(\pi(x - x_p)/FOV)$ [21], where the denominator can be considered constant at a small scale (a few pixels) outside the main lobe. In the context of non-linear phase

distribution, $\Phi(x)$ can be developed to first order, so that the SRF for the pixel p becomes, locally around any position x_c outside from the considered pixel:

$$SRF(x, x_p) = \frac{\exp(i\Phi(x_c))}{N}$$
$$\times \frac{\exp\left(i\frac{\partial\Phi}{\partial x}(x_c) \cdot (x - x_c)\right) \sin\left(\pi N(x - x_p)/FOV\right)}{\sin\left(\pi(x_c - x_p)/FOV\right)}$$
(9)

By definition, the signal contamination in the pixel p originating from a neighborhood of width λ around x_c, normalized by the intrapixel signal $\sim\exp(i\Phi(x_p)) \times FOV/N$, is given by integration of Eq. (9) between $x_c - \lambda/2$ and $x_c + \lambda/2$:

$$\chi(x_c, \lambda, x_p) = e^{i(\Phi(x_c) - \Phi(x_p))} \times \underbrace{\frac{1}{N \sin\left(\pi(x_c - x_p)/FOV\right)}}_{\Gamma}$$
$$\times \Psi\left(x_c - x_p, \lambda, k_{max}, \frac{\partial\Phi}{\partial x}(x_c)\right)$$
(10)

Γ is a slowly varying envelope function accounting for the local envelope of the SRF that does not depend on Φ, while Ψ is the following complex function:

$$\Psi = \frac{ik_{max}\lambda}{2\pi}\exp(-ik_{max}(x_c - x_p))\mathrm{sinc}\left\{\left(\frac{\partial\Phi}{\partial x}(x_c) - k_{max}\right)\frac{\lambda}{2}\right\}$$
$$- \frac{ik_{max}\lambda}{2\pi}\exp(ik_{max}(x_c - x_p))\mathrm{sinc}\left\{\left(\frac{\partial\Phi}{\partial x}(x_c) + k_{max}\right)\frac{\lambda}{2}\right\}$$
(11)

Ψ is a dimensionless 'coherence' function that describes how the oscillations of the nominal SRF integrate incoherently or coherently around x_c over the length λ, when modulated by Φ. If, around a position x_c outside the main lobe of the SRF, spin density varies on a shorter distance than the length λ over which the SRF integrates to zero ($\Psi(\lambda) = 0$), then the signal around x_c is not canceled out and contaminates pixel p. These outer-pixel coherence regions are the same for all pixels (see for example Fig. 1a and b), since the transformation $p \rightarrow p + 1$ only changes the sign of Ψ (however, the relative phase $\Phi(x_c) - \Phi(x_p)$ of contamination signal compared to intrapixel signal is non-linear, so that some non-periodic pattern of dark and bright rows might appear on images). Regarding the magnitude of Ψ, for some combinations of $x_c - x_p$, k_{max} and $\partial\Phi/\partial x$ the SRF can stay coherent over relatively large λ, generating large contamination sources. More precisely, Ψ reaches its highest magnitude when the two exponential terms in Eq. (11) add coherently:

$$|\Psi|_{max} = \frac{k_{max}\lambda}{2\pi}\left(\left|\mathrm{sinc}\left\{\pi\left(\frac{\partial\Phi}{\partial x}\bigg/k_{max} - 1\right)\frac{k_{max}\lambda}{2\pi}\right\}\right|\right.$$
$$\left.+ \left|\mathrm{sinc}\left\{\pi\left(\frac{\partial\Phi}{\partial x}\bigg/k_{max} + 1\right)\frac{k_{max}\lambda}{2\pi}\right\}\right|\right)$$
(12)

$|\Psi|_{max}$ is plotted on Fig. 3a, as a function of $|\partial\Phi/\partial x|/k_{max}$ and $k_{max}\lambda/2\pi$. For each value of $|\partial\Phi/\partial x|/k_{max}$, the maximal value of $|\Psi|_{max}$ (i.e. the envelope of the projection of $|\Psi|_{max}$ along the $|\partial\Phi/\partial x|/k_{max}$ axis) is plotted on Fig. 3b. It appears that the maximal outer-pixel coherence remains low in a very stable manner as long as the following condition is fulfilled:

$$\left|\frac{\partial\Phi}{\partial x}\right| \leqslant 0.3k_{max}$$
(13)

This condition is equivalent to the C_N condition introduced in Eq. (6). For higher values of $|\partial\Phi/\partial x|$ the maximal contamination increases dramatically, resulting in substantial outer-pixel contamination and truncation artifact.

2.4. Spatial apodization using a sliding window

In practice, spatial apodization is usually performed on SI data in order to minimize secondary lobes of the SRF. While signal loss without apodization might be negligible, doubling the FWHM may lead to a dramatic intra-pixel signal loss (Fig. 2). However, for any given pixel in x_p, a filter W_p centered on $(\partial\Phi/\partial x)(x_p)$ can compensate for this sig-
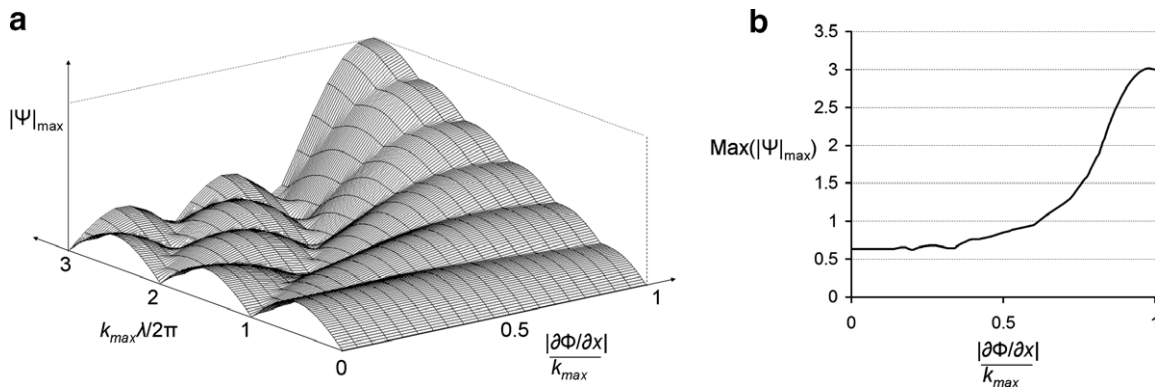

Fig. 3. (a) Maximal outer-pixel coherence $|\Psi|_{max}$, as a function of the phase derivative at the center of the contamination source $|\partial\Phi/\partial x|$ normalized by k_{max}, and of the product of k_{max} by the size λ of contamination area, divided by 2π. (b) The maximal value of $|\Psi|_{max}$ (considering all possible λ) as a function of $|\partial\Phi/\partial x|/k_{max}$ (i.e. the envelope of the projection of (a) on the $|\partial\Phi/\partial x|/k_{max}$ axis), representing the maximal coherence for a given $|\partial\Phi/\partial x|/k_{max}$ ratio.

nal loss, in analogy to the sliding window described by Park et al. [12]. Such a filter provides a SRF locally identical to what would be obtained with the same but centered filter W^0 for the in-phase distribution. As shown in Appendix B, this is due to the fact that a shift of W^0 by an amount $-(\partial\Phi/\partial x)(x_p)$ in the k-space is equivalent to a spatial linear phase $-(\partial\Phi/\partial x)(x_p) \times x$ in the image, which compensates for the local dephasing around x_p and allows full signal to be retained. Note that, since in practice k-space sampling is limited, shifting the apodization window might result in the truncation of the window on one side. However, one-sided truncation of the filter does not degrade the SRF as much as two-sided truncation (Appendix C). The SRF may remain relatively unaffected for shifts higher than $0.3k_{max}$ (depending on the filter used), thus allowing a greater flexibility on the minimal number of phase encodings compared to the C_N condition. For a Hanning window with width $2k_{max}$, shifts such as $0.4–0.5k_{max}$ still yield a relatively unaltered SRF. We ascribe this robustness to one-sided truncation to the fact that high spatial frequencies are still sampled on the other side of the window, so that the spatial resolution does not degrade as much as with two-sided truncation. In the end, the following sliding window algorithm can be applied, for an arbitrary number of spatial dimensions. For each pixel (at position x_p):

- Determine the intrinsic spatial frequency $(\partial\Phi/\partial x)(x_p)$. Such calculation can be done by simulation of the Bloch equations.
- Generate a shifted filter W_p from the centered filter W^0: $W_p(k) = W^0(k - (\partial\Phi/\partial x)(x_p))$.
- Multiply the acquired k-space by the shifted filter W_p, and perform the Fourier transform to yield a temporary image.
- Extract the signal of pixel in x_p in the temporary image, and pad the final image in position x_p with it.

2.5. Echo-time shifting

This section focuses on a spectroscopic issue: the dependence of the spectroscopic echo-time (time when all chemical shifts are in phase) on the position, resulting in spectral distortions (first order phase and baseline oscillations) for pixels where the echo occurs before or after the start of the acquisition.

Let us consider a spectroscopic sequence with a nonselective excitation pulse followed by two unpaired AFP pulses (in conjunction with gradients) generating an echo, TE being the nominal echo-time. Letting the time t be 0 at the beginning of the sequence, after the two pulses, the phase for a given chemical shift δ is given by:

$$\Phi(\delta, t) = -\delta \times (t - TE + 2t_1 - 2t_2) \tag{14}$$

Here t_1 is the time of inversion of the spins during the 1st AFP, and t_2 is the time of inversion during the 2nd AFP, i.e. the time at which the frequency of the pulse matches

the Larmor frequency of the spins ($0 \leqslant t_1, t_2 \leqslant T_p$). In general, given the speed of the frequency sweep, t_1 and t_2 can be considered independent of δ and to be determined by the position only. At a given position, the echo occurs at the time t_{echo} when all chemical shifts have the same phase ($\partial\Phi/\partial\delta = 0$):

$$t_{echo} = TE + 2(t_2 - t_1) \tag{15}$$

When the AFP are paired, $t_2 = t_1$ and the echo occurs at the regular echo-time $t_{echo} = TE$. In the case of two identical AFP pulses selecting a VOI in the X and Z directions, TE is also the time of the echo for the entire diagonal $z = x$, since for that diagonal $t_2 = t_1$. However the time of the echo deviates from the nominal value as the position gets farther from the diagonal. The earliest echo occurs when $t_1 = T_p$ and $t_2 = 0$, corresponding to $t_{echo} = TE - 2T_p$. The latest echo occurs when $t_1 = 0$ and $t_2 = T_p$, i.e. $t_{echo} = TE + 2T_p$. Such a shift of the echo-time by a few ms is sufficient to induce a large 1st order phase and baseline distortion. In order to collect the earliest echo, the acquisition must start $2T_p$ before the nominal echo. Then, after spatial reconstruction, the following echo-shifting algorithm can be applied for each pixel so that all free induction decays (FID) start at the top of the echo:

- Determine the frequency at the center of the pixel during the first pulse and during the second pulse, knowing the gradients during each pulse.
- Determine t_1 and t_2 (time when the frequency of the first and second pulse reaches the frequency at the center of the pixel) and calculate t_{echo} from Eq. (15).
- Remove the corresponding number of points acquired before t_{echo} at the beginning of the FID.

In practice, the earliest echo occurs only on the very edge of the VOI. The echo-shift becomes much smaller as soon as the pixel is not on the very edge. Therefore for a finite pixel size, the maximal echo-shift at the center of the pixel is smaller than $2T_p$ even for the edge pixels, and the acquisition can start less than $2T_p$ before the nominal echo-time.

The sliding window algorithm and the echo-shifting algorithm, respectively performing adequate spatial and spectral post-processing on a pixel-by-pixel basis, will be referred to, when combined, as the 'sliding reconstruction algorithm'.

3. Numerical simulations

3.1. Outer-pixel coherence

While intra-pixel signal loss is quite intuitive, the analysis of outer-pixel coherence derived in Section 2.3 is less straightforward. The goal of the present section is therefore to assess outer-pixel coherence in a 'real' situation of limited Fourier sampling and reconstruction. Let us consider an object as displayed on Fig. 4a, with zero

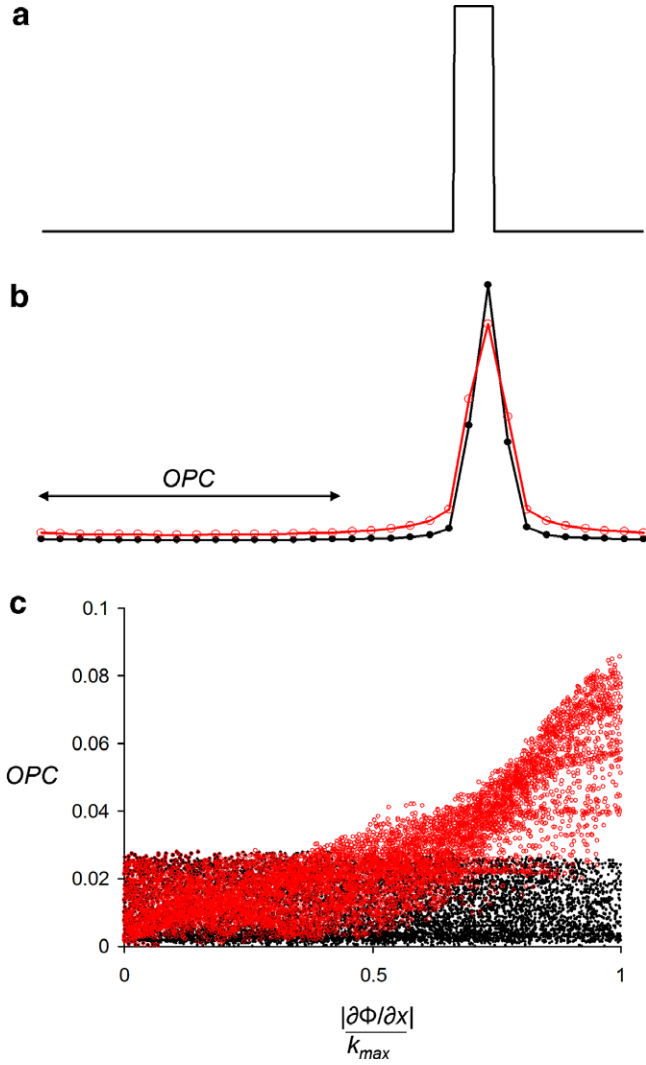**a**

b

OPC

c

OPC

Fig. 4. Numerical evaluation of outer-pixel coherence. (a) Original object with zero density everywhere except in a region of unit density. (b) Reconstructed magnitude image ($N = 32$), for the original object with a quadratic phase $\Phi(x) = 32\pi \times (x/FOV)^2$ (red curve) and without (black curve). $|\partial\Phi/\partial x| = 0.45 k_{max}$ for the unit density region above and this phase distribution. Pixels on the left side of the image exhibit a higher signal when the quadratic phase is applied, showing that the outer-pixel coherence originating from the unit density region is higher. (c) The average signal for pixels on the left side of the image yields the outer-pixel contamination (OPC) as a function of $|\partial\Phi/\partial x|/k_{max}$, obtained by Monte-Carlo simulation (10,000 draws) with random quadratic phase distribution and random unit density region (red open circles), exhibiting a similar pattern as the prediction of Fig. 3B. The black dots stand for OPC calculated for the same Monte-Carlo draws, but with a zero phase distribution.

density everywhere except in a region on the right side of the FOV where density is equal to 1. This region of unit density acts as a signal source contaminating pixels outside this region. A quadratic phase $\Phi(x) = 32\pi \times (x/FOV)^2$ was applied to this object (x being zero at the center of the FOV). The resulting complex distribution was used to generate the corresponding Fourier components for $N = 32$ phase encodings. For comparison with an in-phase distri-

bution, the Fourier components associated with the same distribution, but with $\Phi(x) = 0$, were also calculated. The Fourier reconstructed images (Fig. 4b) clearly show that the signal magnitude on the left side is higher when the object has a non-linear phase, demonstrating higher contamination originating from the unit density region.

A systematic study of outer-pixel contamination as a function of $(\partial\Phi/\partial x)/k_{max}$ was performed using Monte-Carlo simulation (10,000 draws). For each draw, a unit density region was randomly generated in the right half of the FOV. A random number α was chosen and a corresponding quadratic phase distribution $\Phi(x) = \alpha \times (x/FOV)^2$ was applied to the object. Fourier components were calculated for a constant number of phase encodings ($N = 32$), and the image was reconstructed. For comparison, the image was also reconstructed in the case $\Phi(x) = 0$. The signal average for the 16 pixels on the left side of the image was then evaluated, yielding a quantitative measurement of outer-pixel contamination (OPC). For each Monte-Carlo draw, OPC is plotted as a function of $|\partial\Phi/\partial x|/k_{max}$ on Fig. 4c, yielding a very similar pattern as the prediction of Fig. 3b. It appears that OPC starts to increase for $|\partial\Phi/\partial x| > 0.3 - 0.35 k_{max}$, which is in good agreement with the value predicted in Eq. (13).

3.2. The C_N condition for π rotations induced by HS1 pulses

The aim of this part is to validate the expression for the minimal number of phase encodings required to satisfy the C_N condition in the case of HS1 pulses, as predicted in Eq. (7). Evolution of magnetization for a 2D spin distribution was simulated in Matlab (The MathWorks Inc., Natick, MA), using the vectorial formalism of the Bloch equations (excluding relaxation).

Simulation was performed for two orthogonal HS1 pulses ($\beta = 5.3$, $R = 15$). The phase map Φ of the spin distribution allowed the local frequencies $\partial\Phi/\partial x$ (and $\partial\Phi/\partial z$ for the second dimension) to be derived. The number of phase encodings N tested was 0.5×, 1×, 1.5×, 1.75×, 2×, 2.5× and 3× the characteristic number $R \times FOV/THK$ as appearing in Eq. (7), with $FOV/THK = 1.1$. The fraction of the VOI whose frequencies $\partial\Phi/\partial x$ and $\partial\Phi/\partial z$ are less than 30% of k_{max} in both dimensions (C_N condition) was evaluated. Fig. 5 presents these results as a function of N. The fraction reaches 80% of the VOI (90% of the nominal VOI along each dimension) when N is higher than $1.75 R \times FOV/THK$, in excellent agreement with the prediction of Eq. (7).

3.3. Spatial apodization by the sliding window

In order to estimate the efficiency of the sliding reconstruction algorithm, phase encoding was included in the simulation routines. The parameters of the simulation were $R = 15$, $FOV/THK = 1.1$ and 22×22 phase encodings (similar to in vivo experiments), corresponding to $|\partial\Phi/\partial x|$ and $|\partial\Phi/\partial z| \leqslant 0.4 k_{max}$, i.e. an only slight violation
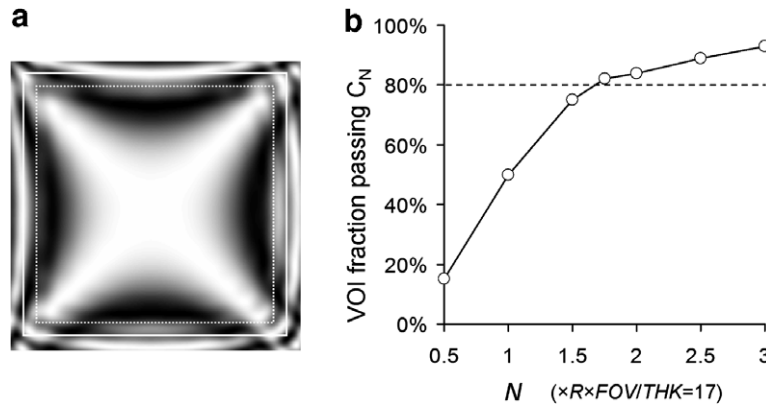
Fig. 5. (a) Simulated phase maps of a uniform spin distribution, for a VOI (white square) localized with two orthogonal unpaired HS1 pulses ($R = 15$). The effective VOI (80% area of the nominal VOI) is marked as a dotted white square. Each black–white step corresponds to a $\pi/2$ phase variation. (b) Fraction of VOI passing the C_N condition (i.e. $\partial\Phi/\partial x$ and $\partial\Phi/\partial z$ are off-centered by less than 30% of k_{max} in both dimensions), as a function of the normalized number of phase encodings $N/(R \times FOV/THK)$, with $FOV/THK = 1.1$.

of the C_N condition compatible with sliding Hanning apodization. The spatial frequencies $\partial\Phi/\partial x$ and $\partial\Phi/\partial z$ used in the sliding window algorithm were determined from the phase map of Fig. 5. The unfiltered image exhibits a pattern of brighter and darker columns and rows (Fig. 6a) characteristic of truncation artifacts. Although a centered Hanning window eliminates this artifact, it induces a signal loss on the edge of the VOI (Fig. 6b). In contrast, a sliding apodization retains signal at the edges of the VOI (Fig. 6c), at least within the effective VOI representing 80% of the nominal VOI (white dotted square on Fig. 6c). More precisely, at the center of the VOI, there is no difference in signal intensity between the images reconstructed with the centered and the sliding algorithm, as expected from the fact that the intrinsic spatial frequencies $\partial\Phi/\partial x$ and $\partial\Phi/\partial z$ are equal to 0. As pixels are farther away from the center, the signal gain becomes higher. Outside the effective VOI, the intrinsic spatial frequencies become rapidly too high for the truncation of the sliding window to be considered negligible, so that reconstruction is not performed correctly (this is the reason for the irregular white and black pixels outside the effective VOI on Fig. 6c).

4. *In vivo* experiments

4.1. Experimental design

Experiments were conducted on a horizontal 9.4 T/31 cm Varian system equipped with a gradient coil reaching 450 mT/m in 200 µs. A surface quadrature coil was used for radiofrequency transmission and reception. Localized first and second order shimming was performed using Fastmap [22]. From previous LASER-localized 2D-SI acquisitions in the rat brain in comparable conditions [6], it was expected that a 0.5×0.5 mm^2 in-plane resolution (with a 3 mm slice thickness) would yield acceptable SNR with ~100 min acquisition time. Taking a FOV/THK ratio of ~1.1 and $THK = 10$ mm (dimension of the rat brain), this leads to $N = 22$. In that context, HS1 pulses with $R = 15$ (corresponding to $|\partial\Phi/\partial x| \leqslant 0.4k_{max}$) were considered optimal for slab selection with minimal chemical-shift localization error (~4%/ppm with the experimental pulse duration $T_p = 1.5$ ms).

A new sequence named Pseudo-LASER (Fig. 7a), derived from the LASER sequence [4], was used to select a $10 \times 3 \times 10$ mm^3 axial slab. Non-selective excitation was
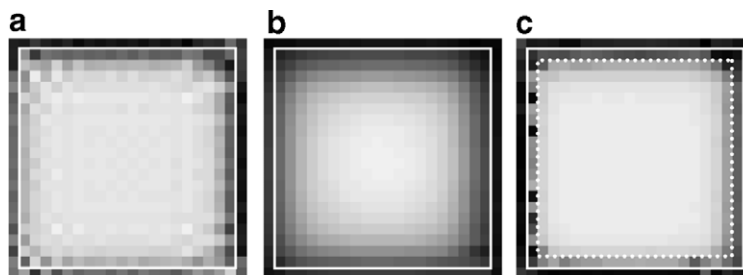

Fig. 6. Numerical simulation of the SI map for a uniform spin distribution localized by two unpaired HS1 pulses ($R = 15$), with $FOV/VOI = 1.1$ and 22×22 phase encodings, illustrating the benefit of the sliding apodization window in terms of signal intensity and homogeneity. (a) Reconstruction without spatial apodization. (b) Reconstruction with the centered spatial apodization window (Hanning). (c) Reconstruction with the sliding spatial apodization (Hanning). The nominal VOI is represented by a continuous white square, while the effective VOI where the spatial apodization is efficient (~80% of the nominal VOI) is represented by a dashed white square.
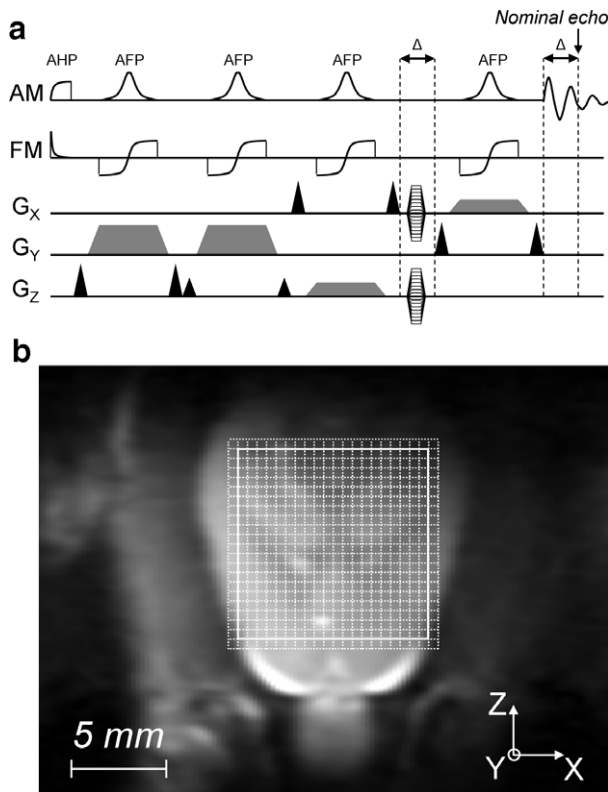
Fig. 7. (a) The Pseudo-LASER sequence with slab selection by paired AFP pulses along Y, and selection by unpaired AFP and phase encoding along the X and Z directions. Amplitude modulation (AM) and frequency modulation (FM) of the RF pulses are displayed. Selection gradients are in gray, crusher gradients are in black. Note the acquisition starting $\Delta = 1.8$ ms before the nominal echo-time, in order to collect the earliest echoes. (b) Position of the $10 \times 3 \times 10$ mm^3 VOI localized by the Pseudo-LASER sequence (continuous lines), and the 22×22 SI matrix (FOV = 11×11 mm^2) (dashed lines).

performed with an AHP, then a pair of AFP pulses (HS1, $R = 25$, $T_p = 1.5$ ms) was used for slab selection along the Y-direction. Finally, two unpaired AFP pulses (HS1, $R = 15$, duration 1.5 ms) were used in parallel with gradients for selection along the X and Z directions. A SI gradient encoding (1 ms duration) in the X and Z directions was included just before the last AFP pulse. With the actual pixel size and pulse duration, the earliest echo occurs only a delay $\Delta = 1.8$ ms before the nominal-echo time, instead of the theoretical shift $2T_p = 3$ ms in the case of an infinitely small pixel size, allowing $2 \times (2T_p - \Delta) = 2.4$ ms to be saved on the nominal echo-time. All sequence delays were reduced to the minimal possible value, so that the acquisition could start just after the crusher gradient following the last AFP pulse, i.e. 10.7 ms after the excitation pulse. With this timing, the nominal TE (echo for pixels at the center of the VOI) was 12.5 ms, and the latest echo occurred 14.3 ms after the excitation.

The FOV of the SI acquisition was 11×11 mm^2, which was spanned by 22×22 phase encodings, resulting in a nominal 0.5×0.5 mm^2 in-plane resolution and a 0.75 μL nominal pixel volume. After Hanning spatial apodization

the effective pixel volume was 3 μL, which is among the highest SI resolution reported *in vivo* [23–25]. The spectral width was 5000 Hz, with 2048 complex data points per FID. Water SI was acquired with one repetition. The water signal was then suppressed using an 8-pulse VAPOR module [26], and metabolite SI was acquired with 6 repetitions, corresponding to a total acquisition time of 97 min with a repetition time TR = 2 s. The whole reconstruction procedure, including the sliding reconstruction algorithm (sliding window by a Hanning filter + echo-time shift), was performed in Matlab. For comparison, SI localized by a standard LASER sequence was also performed. Delays and pulses were identical to the Pseudo-LASER sequence, except that pulses were used in pairs along the X- and Z-axis. The minimal achievable TE in the standard LASER sequence was 19.5 ms.

4.2. In vivo data

A male Sprague–Dawley rat was anesthetized with isoflurane (~1.5%) in O_2/N_2O (30%/70%). Pseudo-LASER was used to select the $10 \times 3 \times 10$ mm^3 axial slab displayed on Fig. 7b. Water SI maps obtained with LASER and Pseudo-LASER are shown in Fig. 8a and b, respectively, the signal intensity being the integral of magnitude of the water resonance. On average, the Pseudo-LASER image exhibits a stronger signal than the LASER image ($+14 \pm 12\%$ within the effective VOI), the noise being identical. This is in good agreement with the ~20% signal gain expected from the 7 ms TE reduction given the short water T_2 in the rat brain at 9.4 T (~40 ms [27]).

Comparing metabolite spectra is less straightforward, due to unavoidable variations in B_0 homogeneity and coil sensitivity during the 200 min required for the acquisition of both LASER and Pseudo-LASER water-suppressed images. However, spectra obtained with LASER and Pseudo-LASER present very similar patterns, as shown for some pixels on Fig. 8c–g. This demonstrates that the reconstruction of *in vivo* Pseudo-LASER data using the sliding reconstruction algorithm yields spatial localization and spectral quality comparable to conventional LASER SI data with standard reconstruction.

The benefits of the sliding reconstruction algorithm in terms of spectra quality are exemplified on Fig. 9, for a pixel close to the edge of the VOI (pixel G of Fig. 8b). The "naïve" reconstruction, i.e. standard apodization by a centered Hanning window and FID starting at the nominal TE, yields a spectrum presenting phase variation over the metabolite ppm range (resonances of N-acetyl-aspartate at 2.01 ppm and of creatine at 3.91 ppm are in antiphase, Fig. 9, bottom spectrum). Correcting for the echo-shift allows restoring a homogeneous phase (Fig. 9, middle spectrum). Finally, the sliding apodization window yields an increased SNR. For example, in the case of pixel F (Fig. 9, top spectrum), the SNR increase is ~40%.
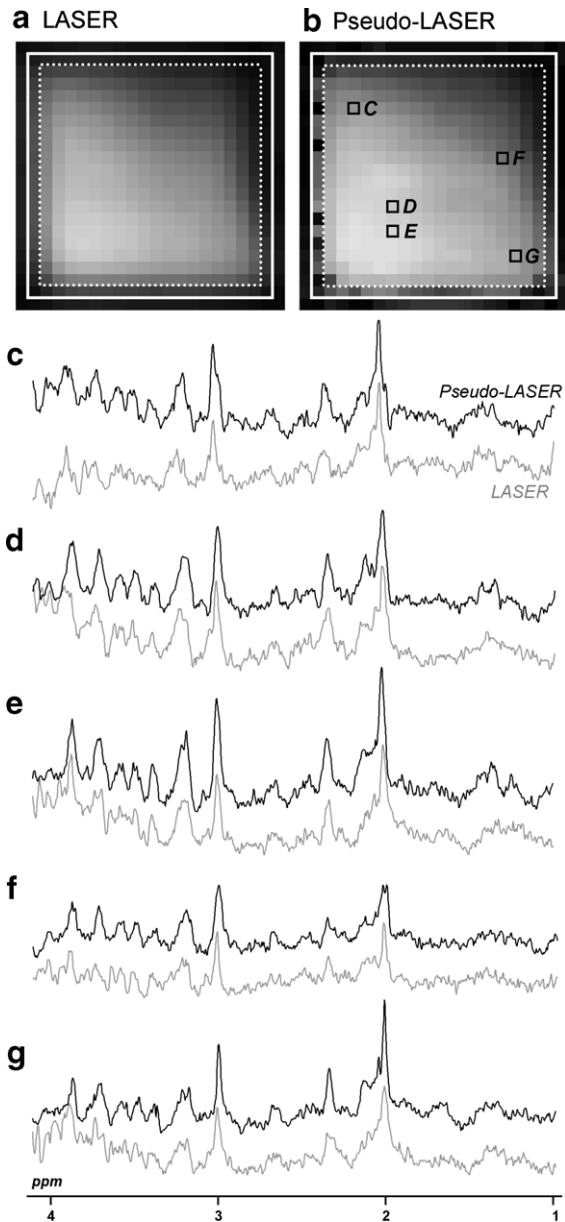
Fig. 8. Comparison of *in vivo* SI (22 × 22 matrix) acquired with LASER and Pseudo-LASER in the VOI displayed in Fig. 7B. (a) Water SI image obtained with LASER (TE = 19.5 ms). (b) Water SI image obtained with Pseudo-LASER (TE = 12.5 ms). The nominal VOI is displayed as a continuous white square, the effective VOI as a dashed white square. (c)–(g) Comparison of spectra obtained in pixels (c–g) with LASER (gray) and Pseudo-LASER (black).
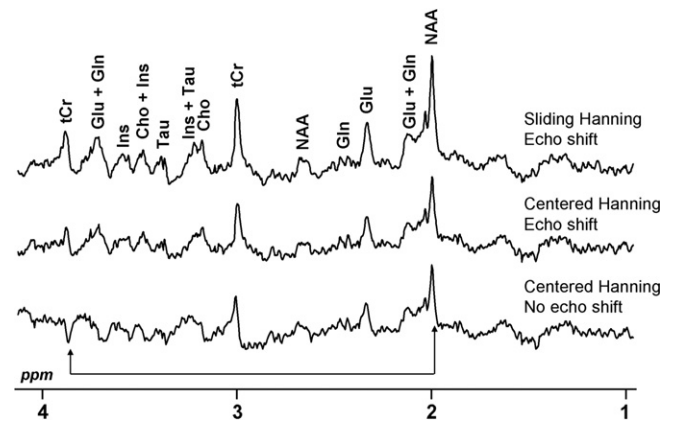
Fig. 9. Effect of the sliding reconstruction for a pixel near the edge of the VOI (pixel G on Fig. 8). (Bottom spectrum) The "naïve" reconstruction, with no echo-shift correction and a centered Hanning window. The resonances of NAA at 2.01 ppm and of tCr at 3.91 ppm are in antiphase. (Middle spectrum) Echo-shifting reconstruction and centered Hanning window. The phase is now constant. (Top spectrum) Full sliding reconstruction (echo-shift + sliding Hanning window), resulting in a gain in SNR of about 40%. Abbreviations used for metabolites are: total creatine (tCr), choline compounds (Cho), glutamate (Glu), glutamine (Gln), inositol (Ins), *N*-acetyl-aspartate (NAA), Taurine (Tau).

5. Discussion and conclusion

This work is a detailed investigation of the specific issues encountered when performing SI with volume selection by unpaired AFP pulses. Theoretical considerations based on how the non-linear phase $\Phi(x)$ affects the SRF yielded the following insights: (1) In the case of a uniform k-space weighting, intra-pixel signal loss is kept smaller than 5% per dimension by adjusting the parameters of the pulse and of the k-space sampling so that $|\partial\Phi/\partial x| \leqslant 0.3k_{max}$ (C_N condition); (2) Outer-pixel coherence is minimized by the same condition, in order to prevent increased truncation artifacts and signal contamination associated with non-linear phase; (3) If truncation artifacts are to be minimized, or if the C_N condition cannot be fulfilled in practice, spatial apodization eliminates outer-pixel coherence by reducing the side lobes of the SRF. However, apodization with a centered filter results in dramatic signal loss on the edges of the VOI, while spatial apodization with a sliding filter allows recovery of the signal, even if the C_N condition cannot be strictly fulfilled (for a sliding Hanning filter $|\partial\Phi/\partial x| \leqslant 0.4 - 0.5k_{max}$ still yields a largely unaffected SRF); (4) The echo-time depends on the position, resulting in phase distortion on spectra. A shifted acquisition scheme was proposed in order to collect and properly process all the echoes. The concepts developed here were further investigated by numerical simulations. Finally, the practical feasibility was demonstrated *in vivo* in the rat brain at 9.4 T using a new sequence named Pseudo-LASER, which is basically a LASER sequence with only one AFP pulse for each direction spatially resolved by Fourier encoding.

Although a few studies have already reported SI with prelocalization by unpaired AFP pulses [15,16], no special reconstruction procedure has been described in these reports. In these studies, four AFP pulses were used in an octagonal pattern, resulting in a partial phase refocusing, so that regular post-processing yielded images with negligible artifact. The present work shows that regular post-processing may not be adequate when two AFP pulses are used for 2D selection.

Special reconstruction procedures have been described previously for MRI with slice selection by unpaired adiabatic pulses. In the case of a quadratic phase as induced

by a CHIRP pulse, it was proposed to localize the signal using a quadratic transformation instead of the Fourier transform [9]. Alternatively, images were reconstructed using conventional Fourier transform by Park et al. [12], and apodization was performed using a sliding window. In both cases, the reconstruction was performed "locally" for each pixel x_p, around a central data point corresponding to the pseudo-echo for that pixel, which is the time when the readout gradient locally compensates for the non-linear phase dispersion induced by the pulse, i.e. the time t_{PE} when $(\partial\Phi/\partial x)(x_p, t_{PE}) = 0$. It is interesting to parallel this concept of pseudo-echo during a read-out gradient, with the concept of intrinsic spatial frequency $\partial\Phi/\partial x$ as introduced in the present work. Although both concepts refer to the same fundamental notion of a local shift of the Fourier components in the k-space, t_{PE} can only be defined for the frequency encoded direction (direction of the read-out gradient), while the general concept of intrinsic spatial frequency is valid for all spatial dimensions, allowing sliding window apodization in 2D or 3D.

Besides the relatively demanding post-processing, the main drawback of SI localized with unpaired adiabatic pulses is the high spatial resolution required to fulfill the C_N condition (conversely, pulses with a lower bandwidth can be used to decrease the minimal number of pixels). Advantages include a shorter achievable TE and lower power deposition. Therefore this localization method may become more beneficial at higher magnetic field, when T_2 become shorter and power deposition increases. In particular, reducing the TE and the number of pulses may prove crucial when performing SI in the human brain at high field, where SAR limitations impose longer pulses with lower γB_1. In parallel, the higher SNR per volume unit at high field should permit a smaller pixel size and therefore an easier fulfillment of the C_N condition. However, the long scan time associated to the required high spatial resolution may limit routine applications for human studies. Although this was not investigated here, the spreading of the signal throughout the k-space might also prove beneficial in terms of SNR in situations where the receiver gain cannot be otherwise optimized, for example when water suppression is poor. All these beneficial characteristics should be enhanced when performing 3D-SI.

Acknowledgements

Appendix A. Analytical evaluation of the C_N condition for HS1

Let us consider an isochromat with Larmor frequency Ω (in rad/s) precessing in the transverse plan, in the reference frame rotating at the central frequency of the RF pulse. The magnetization flips instantaneously at time t_Ω when

$\omega_{RF}(t_\Omega) = \Omega = -\gamma Gx - \delta$, δ being the chemical shift, x the position and G the gradient used for slab selection. Just before the π rotation, the phase of the isochromat is simply $\Phi_\Omega(t_\Omega^-) = \Omega t_\Omega$, while the phase of the pulse is:

$$\Phi_{RF}(t_\Omega) = \int_{t=o}^{t_\Omega} \omega_{RF}(t)\, dt \tag{A.1}$$

The phase of the isochromat just after the π rotation is:

$$\Phi_\Omega(t_\Omega^+) = 2\Phi_{RF}(t_\Omega) - \Phi_\Omega(t_\Omega^-) \tag{A.2}$$

Then the isochromat precesses until the end of the pulse, leading to:

$$\Phi_\Omega(T_p) = 2\Phi_{RF}(t_\Omega) + \Omega(T_p - 2t_\Omega) \tag{A.3}$$

Taking the values of t_Ω and $\Phi_{RF}(t_\Omega)$ as already calculated by Park et al. [12] for HS1, neglecting chemical shift δ ($\delta \ll \pi BW$) and removing all constant terms, the phase at the end of the pulse is:

$$\Phi(x) = -\frac{\pi BW T_p}{\beta} \ln\left(\frac{\pi BW}{\sqrt{(\pi BW)^2 - (\gamma Gx)^2}}\right)$$
$$+ \frac{\gamma G T_p x}{2\beta} \ln\left(\frac{\pi BW + \gamma Gx}{\pi BW - \gamma Gx}\right) \tag{A.4}$$

Using $R = BW \cdot T_p$, defining the thickness of the slab THK such as $2\pi BW = \gamma G \cdot THK$, and introducing the normalized variable $X = 2x/THK$ ($-THK/2 < x < THK/2$ corresponds to $-1 < X < 1$), the phase simply becomes:

$$\Phi(X) = \frac{\pi R}{\beta}\left(\ln\left(\sqrt{1 - X^2}\right) + \frac{X}{2}\ln\left(\frac{1+X}{1-X}\right)\right) \tag{A.5}$$

The derivative of the phase relative to X simplifies to:

$$\frac{\partial\Phi}{\partial X} = \frac{\pi R}{2\beta}\ln\left(\frac{1+X}{1-X}\right) \tag{A.6}$$

$\partial\Phi/\partial X$ is increasing (decreasing if $\beta < 0$) and takes its maximal value for $X \to 1$ ($X \to -1$ if $\beta < 0$). The edges in $X = \pm 1$ are singular points, however, since they correspond to the transition bands, one can limit the analysis to an effective VOI excluding the edges and filling 90% of the total bandwidth. Thus:

$$\frac{\partial\Phi}{\partial X}(X = 0.9) = \frac{\pi R}{2\beta}\ln(19) \tag{A.7}$$

Note that, since $\partial\Phi/\partial X$ is an odd function, when $\beta < 0$ the maximal value $(\partial\Phi/\partial X)(-0.9)$ is identical to that of Eq. (A7) but with a minus sign. In the end, taking $\ln(19) \sim 3$, $|\beta| = 5.3$ and with $dX/dx = 2/THK$, the C_N condition (Eq. (5)) for HS1 is expressed as:

$$N \geqslant \frac{3\pi R}{|\beta|}\frac{FOV}{THK} \approx 1.75R\frac{FOV}{THK} \tag{A.8}$$

Appendix B. Derivation of the sliding apodization window

Writing $IFT_k\{W^0\}$ the inverse Fourier transform of the spatial apodization window W^0 relative to k, the nominal SRF can be written as:

$$SRF^0(x, x_p) = IFT_k\{W^0\}(x_p - x) \quad (B.1)$$

Similarly one gets for the SRF of the complex spin distribution, with a spatial filter W:

$$SRF(x, x_p) = e^{i\Phi(x)} IFT_k\{W\}(x_p - x) \quad (B.2)$$

Let us now search which filter W_p allows having $SRF(x, x_p) = SRF^0(x, x_p)$ for the pth pixel. Introducing $X = x_p - x$, this constraint on W_p can be expressed by equating (B.1) and (B.2):

$$IFT_k\{W_p\}(X) = e^{-i\Phi(x_p - X)} IFT_k\{W^0\}(X) \quad (B.3)$$

Let us develop the phase to the first order. Although this is only valid locally around x_p, the important point here is that only the phase in the vicinity of x_p has to be taken into account, given the usual shape of $SRF^0(x, x_p) = IFT_k\{W^0\}(X)$ for typical filters, which quickly tends to zero when X becomes higher than half the FWHM. Eq. (B3) is therefore essentially equivalent to:

$$IFT_k\{W_p\}(X) = e^{-i\Phi(x_p)} e^{i\frac{\partial\Phi}{\partial x}(x_p)\cdot X} IFT_k\{W^0\}(X) \quad (B.4)$$

The Fourier transform of Eq. (B4) relative to X yields:

$$W_p(k) = e^{-i\Phi(x_p)} \delta\left(k - \frac{\partial\Phi}{\partial x}(x_p)\right) \otimes W^0(k) \quad (B.5)$$

Since the convolution by a Dirac function is equivalent to a shift, Eq. (B5) ultimately leads to:

$$W_p(k) = e^{-i\Phi(x_p)} W^0\left(k - \frac{\partial\Phi}{\partial x}(x_p)\right) \quad (B.6)$$

In the end, the original filter W^0 shifted by $(\partial\Phi/\partial x)(x_p)$ gives rise to a new off-centered filter which ideally (i.e. without truncation) preserves the SRF for the pth pixel.

Appendix C. One-sided truncation of the apodization window

In practice, when reconstructing signal from pixel near the edges of the VOI using the sliding apodization, the filter is off-centered and hence is truncated on one side. To evaluate how this truncation degrades the SRF, the SRF was simulated for different truncations factors, in the case of a Hanning filter and 22 phase encodings (number used *in vivo*). Fig. 10a shows the nominal SRF and the SRF corresponding to a 50% one-sided truncation. From the SRF of one-sided truncated filters, the FWHM (*FWHM*), the height of the main lobe (*HM*) and the height of the highest secondary lobe (*HS*) were derived. Additionally, the integral of the signal within the nominal main lobe (i.e. between $-FWHM/2$ and $FWHM/2$, taking the FWHM of the SRF for the non-truncated filter) was calculated (*S*). In order to show how one sided-truncation compares to two-sided truncation, the same parameters were also derived for two-sided truncated filters. The results are displayed in Fig. 10b. First, one-sided truncation yields a SRF that deviates much more slowly from the nominal SRF compared to two-sided truncation. Second, a one-sided truncation of the Hanning filter up to 50% (corresponding to $|\partial\Phi/\partial x| = 0.5k_{max}$) yields a SRF very close to the nominal SRF, so that the spatial resolution, the intra-pixel signal and the localization accuracy can be considered preserved.
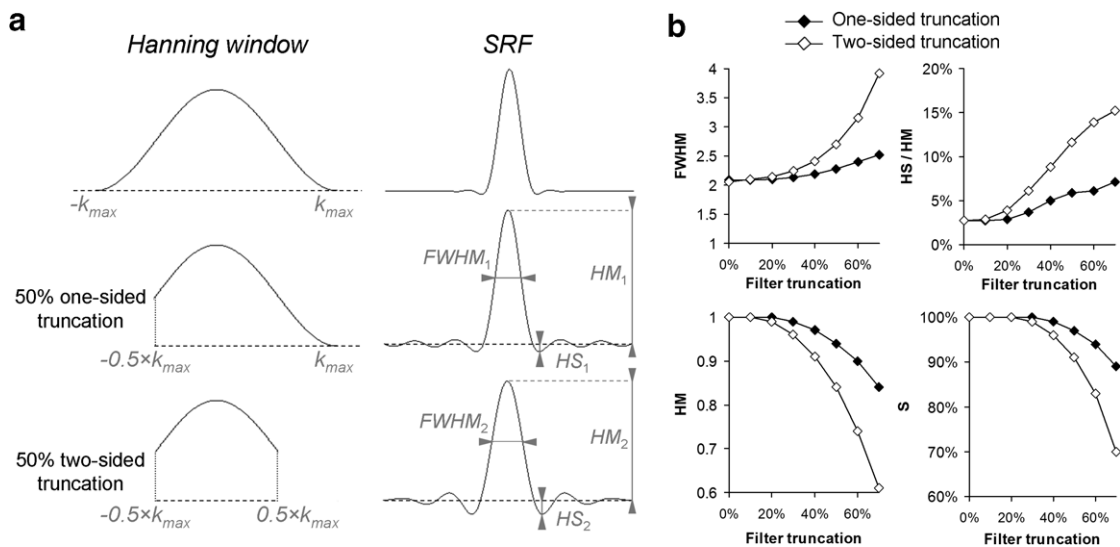

Fig. 10. Effect of truncated apodization window on the SRF. (a) The Hanning filter and the corresponding SRF without truncation of the filter (top row), with a 50% one-sided truncation (middle row) and with 50% two-sided truncation (bottom row). (b) The full-width at half-maximum (*FWHM*), the main lobe height (*HM*), the ratio of the height of the highest secondary lobe *HS* over *HM*, and the integral of the signal within the width of the nominal pixel (*S*), for different truncation factors, in the case of a one-sided truncation (black diamonds) and a two-sided truncation (open diamonds).

In terms of noise, since less noise samples are averaged when integrating under a truncated apodization window compared to a full centered window, the noise standard deviation (SD) decreases. Moreover, since the filter truncation depends on the position, the noise obtained on SI images reconstructed with a sliding apodization window is colored along spatial dimensions, the SD of the noise being smaller on the edges of the image (of course, the noise remains white along the spectral dimension). Note that, since the noise decreases, the decrease in SNR is actually smaller than the signal loss due to truncation (estimated by S).

References

[1] T.R. Brown, B.M. Kincaid, K. Ugurbil, NMR chemical shift imaging in three dimensions, Proc. Natl. Acad. Sci. USA 79 (1982) 3523–3526.

[2] P.A. Bottomley, Spatial localization in NMR spectroscopy in vivo, Ann. N. Y. Acad. Sci. 508 (1987) 333–348.

[3] J. Frahm, K.D. Merboldt, W. Hanicke, Localized proton spectroscopy using stimulated echoes, J. Magn. Reson. 72 (1987) 502–508.

[4] M. Garwood, L. DelaBarre, The return of the frequency sweep: designing adiabatic pulses for contemporary NMR, J. Magn. Reson. 153 (2001) 155–177.

[5] J.A. McNab, R. Bartha, Quantitative short echo-time 1H LASER-CSI in human brain at 4 T, NMR Biomed. 19 (2006) 999–1009.

[6] J. Valette, C. Nelson, I. Iltis, K. Ugurbil, P.G. Henry, High-resolution LASER-localized chemical shift imaging in the rat brain at 9.4 T, Proc. Intl. Soc. Mag. Reson. Med. 15 (2007) 1248.

[7] S. Conolly, G. Glover, D. Nishimura, A. Macovski, A reduced power selective adiabatic spin–echo pulse sequence, Magn. Reson. Med. 18 (1991) 28–38.

[8] T.L. Hwang, A.J. Shaka, Water suppression that works. Excitation sculpting using arbitrary waveforms and pulsed field gradients, J. Magn. Reson. 112 (1995) 275–279.

[9] J.G. Pipe, Spatial encoding and reconstruction in MRI with quadratic phase profiles, Magn. Reson. Med. 33 (1995) 24–33.

[10] O. Gröhn, J. Poduslo, C. Jack, J. Lin, M. Garwood, Adiabatic inner volume selection (IVS) method for high-resolution 3D MRI, Proc. Intl. Soc. Mag. Reson. Med. 11 (2003) 960.

[11] C.R. Jack Jr., M. Garwood, T.M. Wengenack, B. Borowski, G.L. Curran, J. Lin, G. Adriany, O.H. Grohn, R. Grimm, J.F. Poduslo, In vivo visualization of Alzheimer's amyloid plaques by magnetic resonance imaging in transgenic mice without a contrast agent, Magn. Reson. Med. 52 (2004) 1263–1271.

[12] J.Y. Park, L. DelaBarre, M. Garwood, Improved gradient-echo 3D magnetic resonance imaging using pseudo-echoes created by frequency-swept pulses, Magn. Reson. Med. 55 (2006) 848–857.

[13] A.A. Maudsley, Dynamic range improvement in NMR imaging using phase scrambling, J. Magn. Reson. 76 (1988) 287–305.

[14] G. Johnson, E.X. Wu, S.K. Hilal, Optimized phase scrambling for RF phase encoding, J. Magn. Reson. B 103 (1994) 59–63.

[15] O. Gröhn, M. Garwood, A spherical localization method for spectroscopic imaging exploiting adiabatic pulses, Proc. Intl. Soc. Mag. Reson. Med. 10 (2002) 2490.

[16] L.I. Sacolick, D.L. Rothman, R.A. de Graaf, Adiabatic refocusing pulses for volume selection in magnetic resonance spectroscopic imaging, Magn. Reson. Med. 57 (2007) 548–553.

[17] M.S. Silver, R.I. Joseph, D.I. Hoult, Highly selective $\pi/2$ and π pulse generation, J. Magn. Reson. 59 (1984) 347–351.

[18] J. Baum, R. Tycko, A. Pines, Broadband and adiabatic inversion of a two-level system by phase-modulated pulses, Phys. Rev. A 32 (1985) 3435–3447.

[19] D. Kunz, Use of frequency-modulated radiofrequency pulses in MR imaging experiments, Magn. Reson. Med. 3 (1986) 377–384.

[20] A. Tannus, M. Garwood, Adiabatic pulses, NMR Biomed. 10 (1997) 423–434.

[21] Y. Le Fur, A. Ziegler, D. Bourgeois, M. Decorps, C. Remy, Phased spectroscopic images: application to the characterization of the 1H 1.3-ppm resonance in intracerebral tumors in the rat, Magn. Reson. Med. 29 (1993) 431–435.

[22] R. Gruetter, Automatic, localized in vivo adjustment of all first- and second-order shim coils, Magn. Reson. Med. 29 (1993) 804–811.

[23] N. Miyasaka, K. Takahashi, H.P. Hetherington, 1H NMR spectroscopic imaging of the mouse brain at 9.4 T, J. Magn. Reson. Imaging 24 (2006) 908–913.

[24] V. Mlynarik, G. Gambarota, H. Frenkel, R. Gruetter, Localized short-echo-time proton MR spectroscopy with full signal-intensity acquisition, Magn. Reson. Med. 56 (2006) 965–970.

[25] T. Liimatainen, J. Hakumaki, I. Tkac, O. Gröhn, Ultra-short echo time spectroscopic imaging in rats: implications for monitoring lipids in glioma gene therapy, NMR Biomed. 19 (2006) 554–559.

[26] I. Tkac, Z. Starcuk, I.Y. Choi, R. Gruetter, In vivo 1H NMR spectroscopy of rat brain at 1 ms echo time, Magn. Reson. Med. 41 (1999) 649–656.

[27] R.A. de Graaf, P.B. Brown, S. McIntyre, T.W. Nixon, K.L. Behar, D.L. Rothman, High magnetic field water and metabolite proton T1 and T2 relaxation in rat brain in vivo, Magn. Reson. Med. 56 (2006) 386–394.